ACS APPLIED MATERIALS & INTERFACES

Research Article

Cite This: ACS Appl. Mater. Interfaces 2018, 10, 43792−43801

www.acsami.org

Manipulating the Ferroelectric Domain States and Structural Distortion in Epitaxial $BiFeO_3$ Ultrathin Films via Bi Nonstoichiometry

Shilu Tian,[†,‡] Can Wang,*[,†,‡,§] Yong Zhou,[†,‡] Xiaomei Li,[†,‡] Peng Gao,[∥] Jiesu Wang,[†] Yu Feng,[†] Xiaokang Yao,[†,‡] Chen Ge,[†] Meng He,[†] Xuedong Bai,[†,‡] Guozhen Yang,[†,‡] and Kuijuan Jin*[,†,‡,§]

[†]Institute of Physics, Chinese Academy of Sciences, Beijing 100190, China

[‡]University of Chinese Academy of Sciences, Beijing 100049, China

[§]Songshan Lake Materials Laboratory, Dongguan, Guangdong 523808, China

[∥]International Center for Quantum Materials and Electron Microscopy Laboratory, School of Physics, Peking University, Beijing 100871, China

Supporting Information

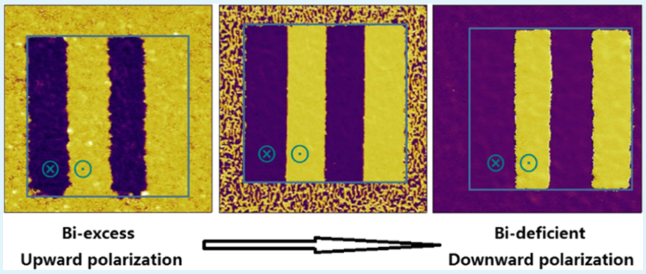

ABSTRACT: Exploring and manipulating domain configurations in ferroelectric thin films are of critical importance for the design and fabrication of ferroelectric heterostructures with a novel functional performance. In this study, $BiFeO_3$ (BFO) ultrathin films with various Bi/Fe ratios from excess Bi to deficient Bi have been grown on $(La_{0.7}Sr_{0.3})MnO_3$ (LSMO)-covered $SrTiO_3$ substrates by a laser molecular beam epitaxy system. Atomic force microscopy and piezoresponse force microscopy measurements show that both the surface morphology and ferroelectric polarization of the films are relevant to Bi nonstoichiometry. More significantly, a Bi-excess thin film shows an upward (from substrate to film surface) uniform ferroelectric polarization, whereas a Bi-deficient thin film exhibits a downward uniform polarization, which means the as-grown polarization of BFO thin films can be controlled by changing the Bi contents. Atomic-scale structural and chemical characterizations and second-harmonic generation measurements reveal that two different kinds of structural distortions and interface atomic configurations in the BFO/LSMO heterostructures can be induced by the change of Bi nonstoichiometry, leading to the two opposite as-grown ferroelectric polarizations. It has also been revealed that the band gap of BFO thin films can be modulated via Bi nonstoichiometry. These results demonstrate that Bi nonstoichiometry plays a key role on the ferroelectric domain states and physical properties of BFO thin films and also open a new avenue to manipulate the structure and ferroelectric domain states in BFO thin films.

KEYWORDS: *$BiFeO_3$ ultrathin films, Bi nonstoichiometry, ferroelectric domain states, structural distortion, interface atomic configuration*

1. INTRODUCTION

Ferroelectrics are widely used in various applications, including sensors, actuators, and memories, for their spontaneous electrical polarization.[1,2] Ferroelectric materials typically form domains during the cooling through the paraelectric−ferroelectric phase transition in order to minimize the total free energy of the system. Not only the domain structures play a role in the ferroelectric properties, but also the domain walls themselves possess exotic properties such as electronic conduction.[3−6] Thus, the effective control of ferroelectric domain configurations is crucial in the ultimate properties of the material. Owing to the strong coupling between the polarization and the charge or lattice degrees of freedom in ferroelectrics, electrical and elastic boundary conditions have a direct effect on ferroelectric domain states. In general, the formation of ferroelectric domains in as-grown ferroelectric thin films relies on the out-of-plane component of the electric displacement field and the in-plane components of the strain at the interface between ferroelectric thin films and substrate.[7] It has been demonstrated that strain[8] and interface electrostatics[9,10] are the key factors to modulate the polarization in ferroelectric thin films.

Multiferroic $BiFeO_3$ (BFO) possesses both strong ferroelectric polarization and G-type antiferromagnetic order at room temperature.[11,12] Bulk BFO has a rhombohedrally distorted perovskite structure with pseudocubic lattice parameters a_r = 3.96 Å and α_r = 89.4°, and ferroelectricity originates from the displacement of Bi ions relative to the FeO_6

Received: September 15, 2018
Accepted: November 26, 2018
Published: November 26, 2018

DOI: 10.1021/acsami.8b15703
ACS Appl. Mater. Interfaces 2018, 10, 43792−43801

octahedra along the pseudocubic [111] direction.[13−15] The polarization can point along any of the four body diagonals of the perovskite unit cell, with two antiparallel polarities for each direction, which can give rise to potentially complicated domain patterns with up to eight possible domain variants. Because of the biaxial strain from the lattice mismatch with the substrate, epitaxial BFO thin films have shown various complex structural distortions, intriguing domain patterns, and novel physical properties.[16−20] Moreover, by exploiting the interfacial valence mismatch and the electrostatic potential step across the interface, Yu et al. have demonstrated that the BFO thin films grown on TiO_2-terminated and SrO-terminated $SrTiO_3$ (STO) substrates have distinct upward and downward polarizations.[10] Therefore, the as-grown polarization directions can be determined by the interface termination with the fine level control of the interface electrostatic potential. In addition, strain gradient (i.e. flexoelectric effect)[21,22] and even defects introduced at specific growth conditions[23] can also affect the domain states of ferroelectric thin films. Nevertheless, the underlying mechanism for domain formation and structure distortion in BFO thin films is yet to be fully understood.

Because of the highly volatile nature of Bi ions at high temperature, Bi-excess BFO compositions in raw materials are often used to fabricate pure-phase and stoichiometric BFO thin films. Actually, BFO thin films often exist in nonstoichiometric compositions accompanied with charge defects such as bismuth, iron, and oxygen vacancies and the valence fluctuation of Fe ions.[24,25] Studies have shown that both the Bi-excess and Bi-deficient nonstoichiometry in BFO thin films have important effects on their physical properties.[25−27] Dedon et al. have observed that the BFO thin films with Bi-deficient and Bi-excess compositions exhibit significant differences in surface and domain morphology, and especially the Bi-deficient BFO thin films show stabilized atomically smooth surfaces and ordered stripe domains.[27] Ultrathin BFO thin films have attracted a lot of attention for their potential applications in multiferroic and ferroelectric tunnel junctions.[28−30] In this work, we focus on the effect of Bi nonstoichiometry on the as-grown polarization states in epitaxial BFO ultrathin films on $(La_{0.7}Sr_{0.3})MnO_3$ (LSMO)-covered STO substrates. Bi-excess BFO thin films show a uniform upward polarization (from substrate to film surface), whereas with the decrease of Bi/Fe ratio, nearly stoichiometric BFO thin films are obviously in the multidomain state with both upward and downward polarizations randomly, and surprisingly, the most Bi-deficient BFO thin film exhibits a uniform downward polarization. Different structural distortions and interface terminations have been revealed for Bi-excess and Bi-deficient BFO thin films, respectively, which should be responsible for the formation of opposite uniform ferroelectric domains.

2. EXPERIMENTAL SECTION

2.1. Growth of Thin Films. BFO ultrathin films with various Bi nonstoichiometry were grown on LSMO-covered (001) STO substrates using a laser molecular beam epitaxy system (Laser-MBE). BFO ceramic targets with various nominal Bi/Fe ratios of 1.5, 1.3, 1.1, 1.0, 0.9, and 0.8 were used to achieve different Bi contents in the BFO thin films. An XeCl excimer laser with the wavelength of 308 nm was employed to irradiate the ceramic targets at an energy density of 1.5 J/cm^2 and a repetition of 2 Hz. The STO substrates were etched by buffered hydrofluoric acid and annealed in flowing oxygen to get the atomic flat TiO_2-terminated surface. During the growth of BFO thin films, the substrate was kept at 630 °C, and the oxygen pressure in the chamber was 15 Pa. The thickness of all the BFO thin films was controlled to be 10 nm by the number of laser ablation pulses, and before the deposition of BFO, a 20 nm-thick LSMO layer was deposited at 800 °C and 30 Pa as the bottom electrode layer. Corresponding to the targets, the BFO thin films were labeled as BFO1.5, BFO1.3, BFO1.1, BFO1.0, BFO0.9, and BFO0.8, respectively, in this paper.

2.2. X-ray Diffraction Measurements. X-ray diffraction (XRD) (θ−2θ scan) measurements were performed to identify the phase structure of BFO thin films by a Rigaku SmartLab (9 kW) high-resolution (Ge 220 × 2) X-ray diffractometer with 1.5406 Å X-rays.

2.3. Atomic Force Microscopy and Piezoresponse Force Microscopy Measurements. The surface morphology and ferroelectric domain configurations were characterized by a commercial atomic force microscope (Asylum Research, MFP-3D). The images were collected using Pt-coated silicon tips with a nominal spring constant of ∼2 N/m and a free-state resonance frequency of ∼70 kHz.

2.4. High-Resolution Scanning Transmission Electronic Microscopy and Atomically Resolved Energy-Dispersive X-ray Spectroscopy Map Measurements. To identify the atomic structures of BFO thin films, high-resolution aberration-corrected scanning transmission electronic microscopy (STEM) of high-angle annular dark field (HAADF) was employed. HAADF imaging was performed on an ARM-300 (JEOL) scanning transmission electronic microscope operated at 300 keV with double-spherical aberration (Cs) correctors. The collection angle for HAADF images is 54−220 mrad. The atomically resolved energy-dispersive X-ray spectroscopy (EDXS) maps were also recorded to determine element distribution at the interface.

2.5. Second-Harmonic Generation Measurements. Second-harmonic generation (SHG) measurements were carried out in a general reflection geometry. The central wavelength of the incident laser is 800 nm with a pulse duration of 120 fs and a repetition of 82 MHz. The angle between incident light and sample normal was set to 45°, and the polarization angle of the incident light can be regulated by a half-wave ($\lambda/2$) plate assembled on a stepping motor controlled by a computer. The SHG intensities as a function of polarization angle of the incident light were recorded in P-out and S-out configurations that denote the analyzer polarization parallel and perpendicular to the plane of incidence, respectively.

2.6. Raman Spectroscopy Measurements. Ultraviolet polarized Raman spectroscopy was studied using a HORIBA HR Evolution 800 Raman spectrometer with a laser wavelength of 325 nm in a back scattering geometry. The excitation laser spot was about 0.5 μm and the incident laser power was kept at 1 mW.

2.7. Spectroscopic Ellipsometry Measurements. The optical properties of thin films were characterized using a dual rotating-compensator spectroscopic ellipsometer RC-2 (J. A. Woollam) with a focus prober around 400 μm in the spectral range from 193 to 1000 nm. The data were acquired at different incident angles from 50 to 75° in steps of 5° to increase the accuracy. The ellipsometry parameters Ψ and Δ, related to the amplitude ratio and the phase difference between the p-polarized and s-polarized reflected light, respectively, were well fitted with an air/BFO/LSMO/STO multilayer optical mode.

3. RESULTS AND DISCUSSION

3.1. XRD and Compositional Characterization. BFO thin films with various Bi/Fe ratios were epitaxially grown on LSMO-covered (001) STO substrates by laser molecular beam epitaxy. The variation of Bi/Fe ratios in BFO films was controlled by using different BFO ceramic targets described in the Experimental Section. Figure 1 shows the XRD θ−2θ scan results for BFO thin films with various Bi/Fe ratios. Besides the STO substrate and LSMO bottom layer, the BFO thin films only exhibit (00*l*) diffraction peaks, suggesting an epitaxial growth without signature of any impurity. (For convenience, the pseudocubic notation is used throughout the text.) Despite

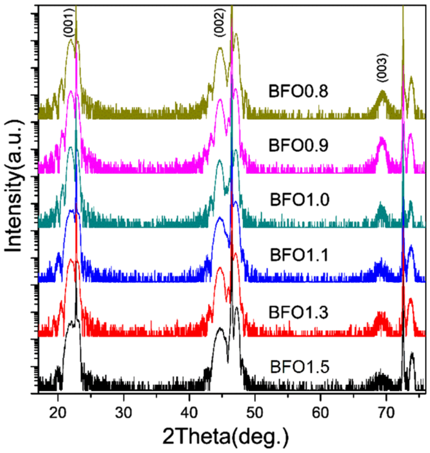

Figure 1. XRD θ−2θ patterns for BFO ultrathin films on LSMO-covered STO substrates deposited using ceramic targets with nominal Bi/Fe ratios from 1.5 to 0.8. The (00*l*) reflection peaks for BFO thin films are marked.

the variation of Bi/Fe ratios, the diffraction peaks of the films have no obvious change in the peak position or shape, which means all the films have a similar lattice constant and crystal quality. Compared with the bulk BFO, the BFO thin films show the (00*l*) diffraction peaks at a lower value of 2θ, indicating that the ultrathin films have an elongation in the out-of-plane lattice parameter, induced by the in-plane compress stress from the substrate. The calculated out-of-plane lattice constant c for the 10 nm-thick BFO thin films is about 4.06 Å, which is equal to that of the films grown on $SrRuO_3$-covered STO[31] and much larger than the value of 3.96 Å for bulk BFO. In terms of epitaxial growth, a c/a lattice constant ratio can be estimated to be 1.04, which is consistent with the maximum values reported for BFO ultrathin films epitaxially grown on STO.[32,33] For BFO thin films epitaxially grown on STO, when the thickness is thinner than 30 nm, it is in a fully strained state with a maximum out-of-plane lattice parameter.[34] Thus, the present 10 nm-thick epitaxial BFO thin films should be in a fully strained state.

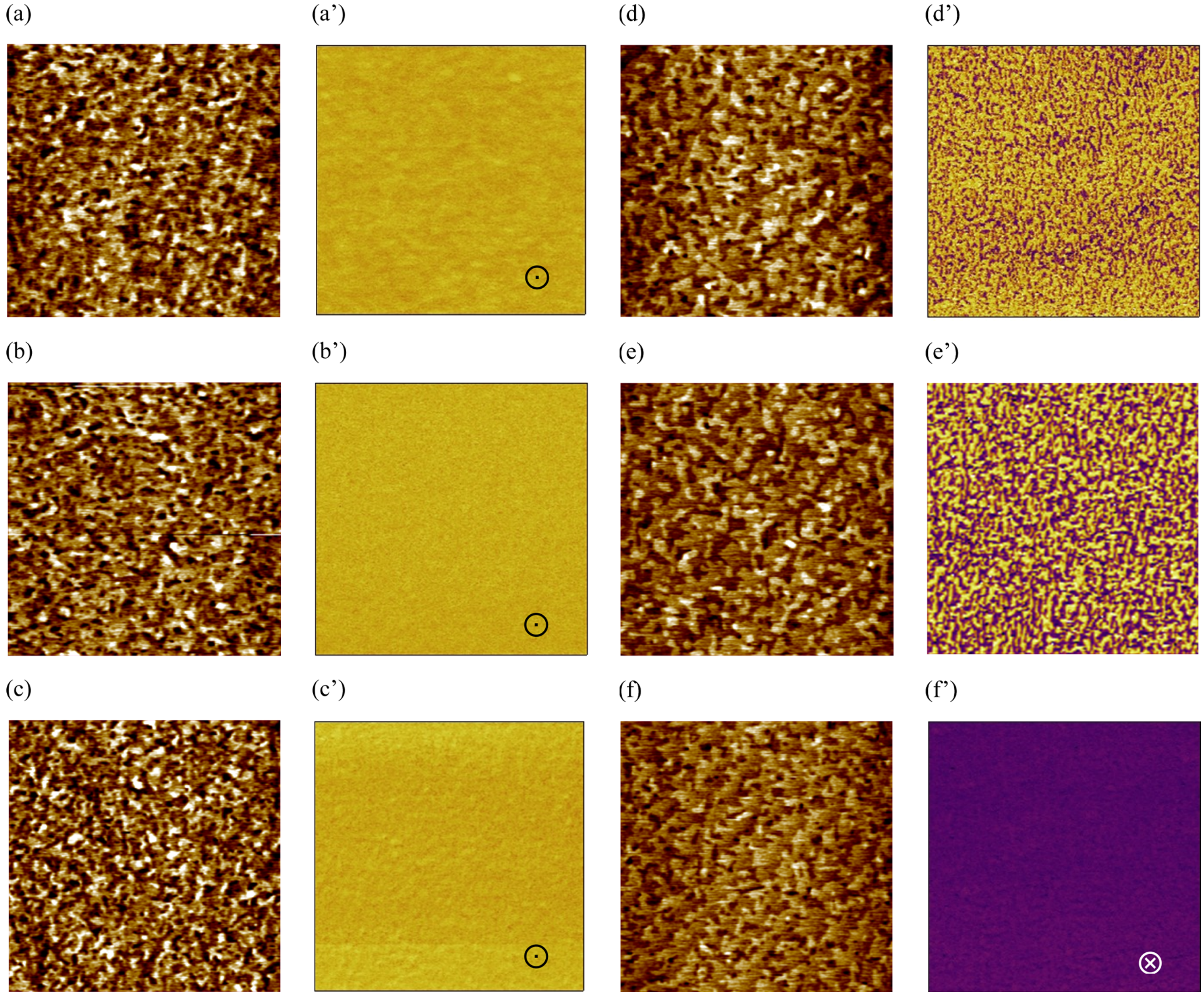

Figure 2. AFM surface topography (a−f) and PFM (a′−f′) images for BFO1.5, BFO1.3, BFO1.1, BFO1.0, BFO0.9, and BFO0.8 ultrathin films. All the images are in a size of 2 × 2 μm^2. The topography images have a scale bar in the range of ±400 pm, and the PFM phase images have a scale bar of 0−200°.

To know the actual Bi/Fe ratios in the thin films and ceramic targets, chemical composition analyses have been performed for them by X-ray photoelectron spectroscopy (XPS) and energy-dispersive spectrum, respectively. The BFO thin films show expected Bi-excess or Bi-deficient compositions with Bi/Fe ratios from 1.02 to 0.96, and interestingly, all the thin films are slightly off-stoichiometry rather than those of the targets from 1.25 to 0.78 (Table S1). It needs to be mentioned that the BFO0.9 and BFO0.8 thin films have Bi/Fe ratios larger than those in the corresponding ceramic targets. This result should be caused by the different ablation rate for Bi and Fe elements, indicating that more bismuth element, compared to iron, would be ablated out by the pulsed laser ablation during deposition. For the same reason, we found that the Bi/Fe ratio in the ablated surface of a BFO ceramic target was decreased dramatically after long-term use for laser ablation. In addition, the results for Bi-excess samples show that even more Bi content can be ablated out from the ceramic targets, the Bi content remained in the single-phase BFO thin films is not so much and it is just close to the stoichiometry composition. This can be related to a self-regulation process,[35,36] and part of the Bi content might be wasted by volatilization. Actually, apart from the factor of target composition, to get high-quality pure phase or stoichiometric BFO thin films, many other parameters[37,38] need to be optimized and well controlled, such as substrate strain, substrate temperature, oxygen pressure, laser energy and frequency, target density, target—substrate distance, and so forth. For example, low temperature and high oxygen pressure conditions can reduce the volatility of Bi, whereas the opposite conditions lead to the larger loss of Bi and result in the formation of iron oxide in BFO thin films.[39,40] To guarantee the attainment of high crystallinity and pure phase of BFO thin films, the slight off-stoichiometry BFO thin films have been fabricated with our optimized deposition conditions. Our results indicate that, by using either Bi-excess or Bi-deficient BFO targets, BFO thin films can be epitaxially grown in a single-phase crystal structure with slight Bi nonstoichiometry, which can be ascribed to the different ablation rate for Bi and Fe elements and a self-regulation process during the film growth.[36,40] Undoubtedly, the Bi nonstoichiometry in the BFO thin films would result in microstructural defects that may have a significant impact on physical properties, which is not detectable by the above analyses. By the way, the valence states of Fe ions analyzed by X-ray absorption spectroscopy and XPS are very close to be trivalent in all the thin films and has a slight increase with the Bi/Fe ratio decrease (Figure S1).

3.2. Evolution of Surface Topography and Ferroelectric Domains with Bi Nonstoichiometry. Figure 2a−f shows the atomic force microscopy (AFM) images of BFO ultrathin films to demonstrate the evolution of surface morphology with the Bi/Fe ratio. All the BFO thin films maintain an atomically flat surface in terms of the small root-mean-square (rms) roughness around 0.2 nm, and the roughness shows a slight increase with increasing Bi/Fe ratio. A discernable terrace-like surface can be observed for Bi-deficient BFO0.8, BFO0.9, and BFO1.0 thin films, whereas the terrace-like surface is gradually damaged with the increase of Bi/Fe ratio. It needs to be mentioned that all the BFO thin films were grown on TiO_2-terminated STO substrates with the clear and regular unit-cell step-and-terrace surface obtained with etching and thermal annealing process,[31] and the surface of the bottom LSMO layer was almost identical to that of the underlying STO substrate (Figure S2). The Bi-deficient BFO thin films show the terrace-like surface, which are corresponding to that of the LSMO/STO and STO substrates. The observed terrace-like surface indicates a layer-by-layer growth mode without the formation of three-dimensional islands, which can be ascribed to the coherently epitaxial growth at the fully strained state. In other words, the Bi-deficient compositions might facilitate the layer-by-layer epitaxial growth of BFO films. The evolution of surface morphology of BFO thin films with Bi/Fe ratios is consistent with the observation in a reported work, wherein the morphology of Bi-deficient BFO thin films exhibit atomic-level terraces and steps, but upon increasing the Bi composition, the rms roughness increases.[27]

Out-of-plane piezoresponse force microscopy (PFM) images of BFO thin films are shown in Figure 2a′−f′, respectively. It is observed that the as-grown ferroelectric domain of the thin films has a great evolution from a uniform upward polarization in the Bi-excess thin films to a uniform downward polarization in the most Bi-deficient thin film. (Upward means the polarization pointing from the substrate to the surface, and downward means from the surface to the substrate, denoted as ⊙ and ⊗, respectively, in this paper.) The Bi-excess BFO1.5, BFO1.3, and BFO1.1 thin films clearly show the uniform upward polarization, and the Bi-deficient BFO0.8 thin film shows the uniform downward polarization, while the less deficient BFO1.0 and BFO0.9 thin films exhibit both upward and downward polarizations randomly distributed in an obviously multidomain state. To demonstrate the switchable ferroelectricity of ultrathin films, four strip domains were written on the thin films in a $1.5 \times 1.5\ \mu m^2$ square by PFM scanning with tip voltages of +5, −5, +5, and −5 V, respectively. Figure 3a−f shows the written domains for BFO1.3, BFO0.9, and BFO0.8 thin films and the corresponding amplitude images. This confirms the ferroelectricity for all the thin films and further validates the as-grown domain orientations. The observed evolution of ferroelectric domain states with Bi nonstoichiometry indicates conclusively that the as-grown polarization of the BFO thin films can be controlled by changing the Bi contents.

3.3. Atomic-Scale Structural and Chemical Characterization at the Interface. To have an insight into the formation of as-grown polarization in BFO thin films, aberration-corrected STEM measurements have been performed for upward polarization Bi-excess BFO1.3 and downward polarization Bi-deficient BFO0.8 samples. Low-magnification cross-sectional STEM images (Figure S3) show the clear interfaces and expected thickness for the BFO (10 nm)/LSMO (20 nm) heterostructures on STO substrates. Figure 4a,b shows high-resolution HAADF STEM images of the BFO/LSMO interfaces for BFO1.3 and BFO0.8, respectively. The images show the brighter BFO layer and a relatively darker LSMO layer based on the difference of atomic numbers of the elements, and both the heterostructures have atomically sharp BFO/LSMO interfaces. Above the interface, the brighter dots in the images correspond to the heavier Bi ions and the weaker dots correspond to the lighter Fe ions. For the Bi-excess BFO1.3 thin film, as shown in Figure 4a, first, we can see a slight tilt or distortion in the (101) plane above the interface. In other words, the angle β between lattice vectors $\mathbf{a}$ and $\mathbf{c}$ is not equal to 90°. Second, the magnified image in the inset shows an upward polarization along the pseudocubic diagonal direction according to the atomic displacement of the

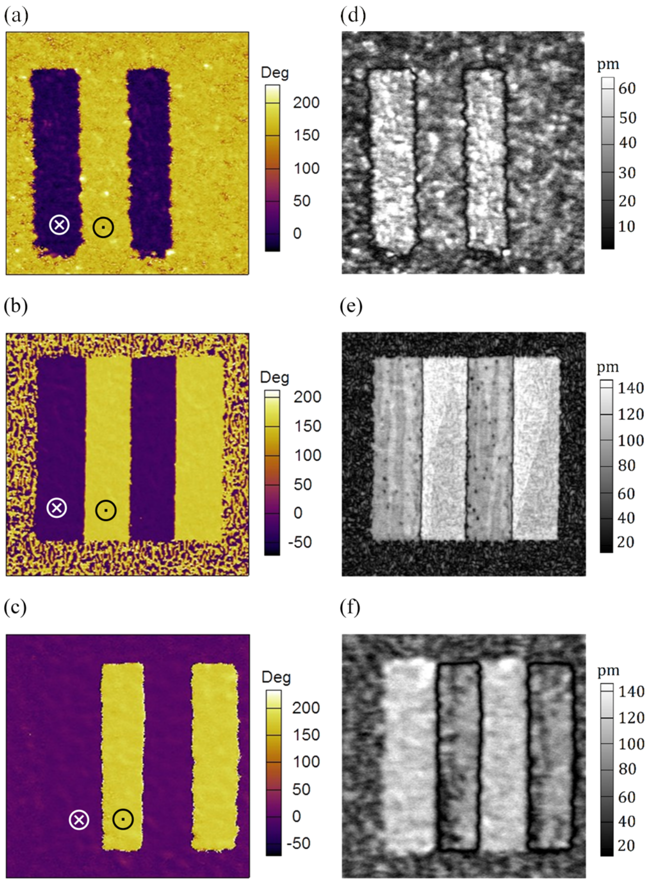

Figure 3. Ferroelectric polarization switching. (a−c) PFM phase images of the written domains. (d−f) Corresponding amplitude images for BFO1.3, BFO0.9, and BFO0.8, respectively. All the images are in a size of 2 × 2 μm^2.

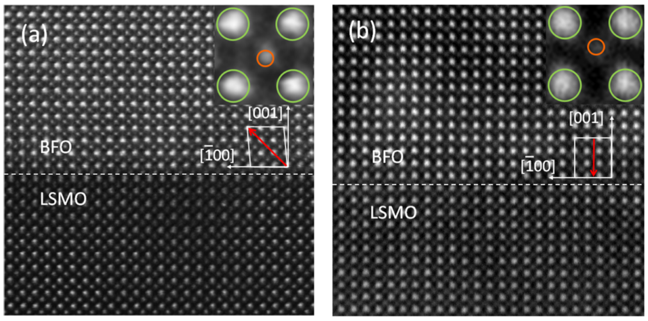

Figure 4. HAADF STEM images of (a) BFO1.3/LSMO and (b) BFO0.8/LSMO along the [010] zone axis. The insets show the magnified images to display the unit cells (where green circles represent Bi atoms, whereas brown circles represent Fe atoms, the relative displacement of Fe atom with respect to the center of four surrounding Bi atoms is in the opposite direction of the polarization) and the schematics to describe the lattice tilt and polarization. Red arrows indicate the polarization direction, and white dotted lines indicate the interface between BFO and LSMO.

Bi cation relative to the Fe sublattice. Both the observations suggest a monoclinically distorted structure for the Bi-excess BFO1.3 thin film. In contrast, for the Bi-deficient BFO0.8 thin film, the STEM image in Figure 4b does not show the tilt and the angle β is a right angle. The magnified image in the inset shows a downward polarization with a near-vertical atomic displacement. These imply a tetragonal-like structure for the Bi-deficient BFO0.8 thin film. Therefore, the STEM images reveal that the Bi-excess BFO1.3 and the Bi-deficient BFO0.8 thin films have different polarization orientations and crystal structures. The different polarization directions for the two samples are further confirmed by the polarization maps calculated by the relative displacements of each atom with respect to the center of four surrounding atoms, which are consistent with the PFM measurements, whereas the evolution of structural distortion is to be further discussed with more information in Section 3.4.

Atomic-scale characterization of chemical composition across the oxide interfaces is important for understanding the physical properties of epitaxial oxide heterojunctions. Atomically resolved EDXS in aberration-corrected STEM has been performed to clarify element distribution at the interface of BFO/LSMO heterostructures. Figure 5 shows the EDXS

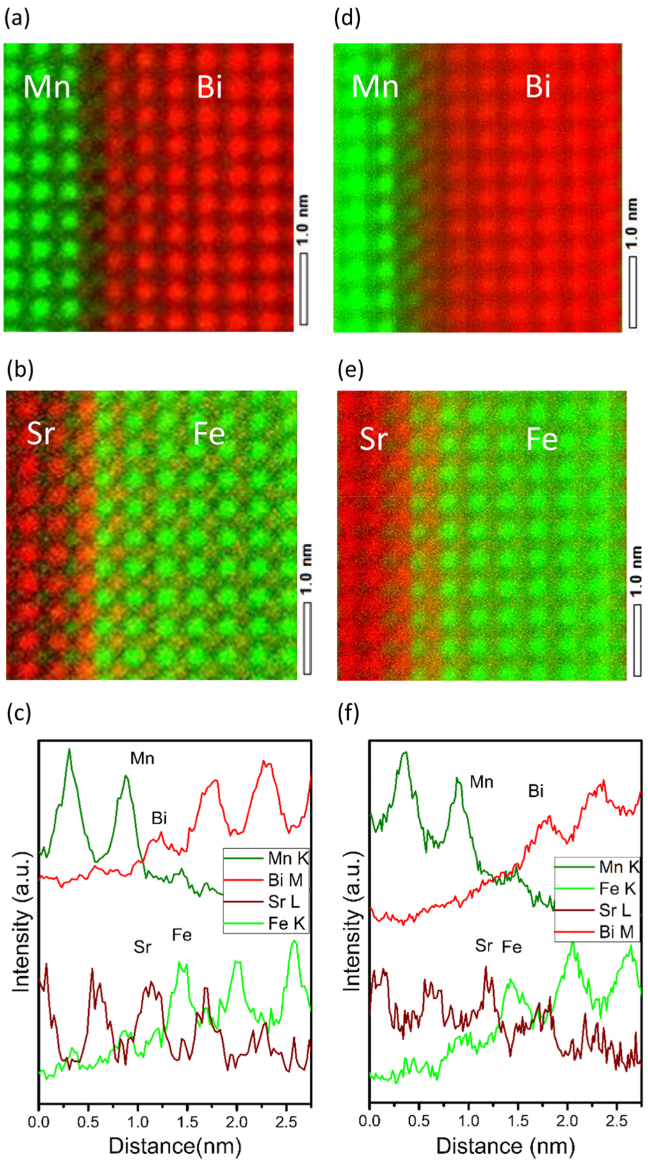

Figure 5. EDXS elemental maps and line profiles crossing the BFO/LSMO interface. (a) Mn- and Bi-combined map, (b) Sr- and Fe-combined elemental map, (c) line profiles for the BFO1.3 thin film, (d) Mn- and Bi-combined elemental map, (e) Sr- and Fe-combined map, and (f) line profiles for the BFO0.8 thin film.

DOI: 10.1021/acsami.8b15703
ACS Appl. Mater. Interfaces 2018, 10, 43792−43801

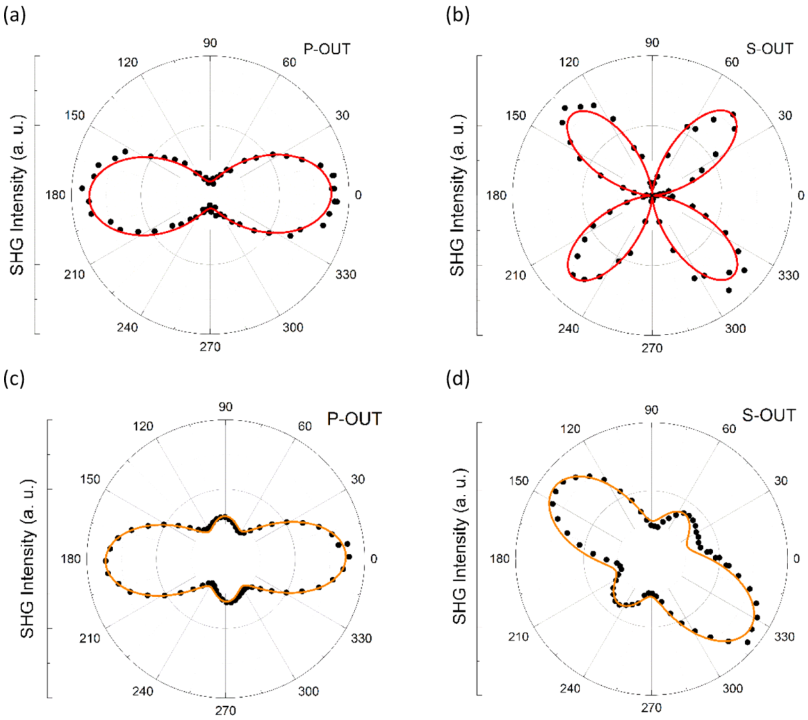

Figure 6. SHG intensities as a function of polarization angle of the incident light, recorded in P-out and S-out configurations, respectively. (a,b) BFO0.8 thin film; (c,d) BFO1.3 thin film. Black dots denote the experimental data and solid lines represent the theoretical simulated data by using a tetragonal structure for BFO0.8 and a monoclinic structure for BFO1.3, respectively.

elemental maps and the line profiles crossing the BFO/LSMO interface for the BFO1.3 and BFO0.8 samples. Figure 5a,d shows the Bi- and Mn-combined elemental maps for the two samples, respectively, both of which show a dimmed gap at the interface, whereas the Sr- and Fe-combined elemental maps in Figure 5b,e show a relatively sharp interface for both the samples. There are two possible interface configurations in the [001]-oriented BFO/LSMO heterostructures, namely, $(MnO_2)^{0.7-}-(BiO)^{1+}$ (for MnO_2-terminated interface) and $[(La_{0.7}Sr_{0.3})O]^{0.7+}-(FeO_2)^{1-}$ (for $La_{0.7}Sr_{0.3}O$-terminated interface). Generally, the existence of the gap between Mn and Bi elements at the interface of BFO/LSMO excludes the interface termination configuration of $(MnO_2)^{0.7-}-(BiO)^{1+}$ and suggests that $[(La_{0.7}Sr_{0.3})O]^{0.7+}-(FeO_2)^{1-}$ is the interface termination configuration on account of the −A−B−A−B− stacking sequence in ABO_3 perovskite structures. To clearly demonstrate the interface chemical composition, the line profiles of the EDXS maps are shown in Figure 5c,f. The profile lines have been taken along the diagonal direction at the BFO/LSMO interfaces. For the Bi-excess BFO1.3 sample, the profile line of Bi in Figure 5c shows a lower peak close to the Mn peak with an interval about 0.28 nm, which is equal to one half of the face diagonal length of a unit cell, indicating that the interface termination formed by $(MnO_2)^{0.7-}$ and $(BiO)^{1+}$ layers are observed. In comparison, for the Bi-deficient BFO0.8 sample, the closest Bi and Mn peaks shown in Figure 5f have a larger interval about 0.85 nm corresponding to one and a half of the face diagonal length; therefore, Bi and Mn could not be the nearest cations for each other and the interface termination would be completely formed by $[(La_{0.7}Sr_{0.3})O]^{0.7+}-(FeO_2)^{1-}$. The interface termination is usually determined by the chemical termination of the substrate,[10] but the two different interface configurations have been observed in our BFO/LSMO heterostructures with the same TiO_2-terminated STO substrates, which is undoubtedly related to the Bi nonstoichiometry in the films. According to the previous reports,[9,10] it is reasonably expected that Bi ions appear at the interface layer of BFO/LSMO on TiO_2-terminated STO. However, for the Bi-deficient BFO sample, Fe ions are located at the interface layer, which would be induced by ion diffusion or other unrevealed mechanisms during the growth of BFO thin films. This result indicates that the Bi/Fe ratio in BFO has direct influences on the interface configurations and can be used to modify the interface configuration of BFO heterostructures.

The electrostatic potential at the interface induced by interfacial valence mismatch is one of the important factors to determine the physical properties of oxide heterostructures.[41] Studies by Yu et al.[9,42] have shown that the BFO on MnO_2-terminated LSMO has an upward polarization because of the $BiO-MnO_2$ interface, and the BFO on (LaSr)O-terminated LSMO has a downward polarization for the $FeO_2-(La,Sr)O$ interface. This has been interpreted in terms of the existence of two different interface dipoles at the BFO/LSMO interface by the polar discontinuity mechanism. The interface polar discontinuity or valence mismatch is mainly screened through the Thomas−Fermi screening in the metallic LSMO layer; thus, the spatial separation between the interface charge and screening charge will lead to an interface dipole at the interface. Therefore, the upward and downward interface dipoles will be formed for the $(MnO_2)^{0.7-}-(BiO)^{1+}$ and $[(La_{0.7}Sr_{0.3})O]^{0.7+}-(FeO_2)^{1-}$ interfaces, respectively. These interface dipoles can develop into an electrostatic potential barrier across the interface and further influence the polarization states in the ferroelectric layer.[9,42] In our case, the observed $(MnO_2)^{0.7-}-(BiO)^{1+}$ interface should contribute to the upward polarization in the Bi-excess BFO1.3, and the $[(La_{0.7}Sr_{0.3})O]^{0.7+}-(FeO_2)^{1-}$ interface will be responsible for

DOI: 10.1021/acsami.8b15703
ACS Appl. Mater. Interfaces 2018, 10, 43792−43801

the downward polarization in the Bi-deficient BFO0.8. As a result, the two different interface atomic configurations of $(MnO_2)^{0.7-}-(BiO)^{1+}$ and $[(La_{0.7}Sr_{0.3})O]^{0.7+}-(FeO_2)^{1-}$ have been observed for the Bi-excess BFO1.3 and Bi-deficient BFO0.8 samples, respectively. The origin of the opposite polarization for the BFO1.3 and BFO0.8 samples can be attributed mainly to the different interface terminations.

3.4. Structural Information from SHG Measurements and Raman Spectra. SHG is a nonlinear optical process in which an incident light with an electric field E and a frequency ω interacts with a nonlinear material and induce a polarization P at frequency 2ω. The induced frequency-doubled light wave can be expressed by $P(2\omega) = \varepsilon_0\chi E(\omega)E(\omega)$, where χ is a tensor as SHG susceptibility. SHG occurs in materials that lack inversion symmetry and hence χ is sensitive to local polar order and structural symmetry. Thus, SHG has become a useful tool for probing ferroelectricity and determining the ferroelectric domain states and structural symmetry by modeling of the polarimetry data.[43−45] To get further structural information of BFO thin films, SHG measurements were carried out in a general reflection geometry as described in detail in ref 46. SHG intensities as a function of polarization angle of the incident light, recorded in P-out and S-out configurations, respectively, are shown in Figure 6. The observed SHG signal indicates the existence of ferroelectric phase, whereas the distinctly different SHG patterns for the two samples imply two different symmetric structures for them. The s-out SHG feature is 4-fold symmetric with peaks appearing at ∼45, ∼135, ∼225, and ∼315° for BFO0.8, as shown in Figure 6b. However, the 4-fold symmetry degrades into a 2-fold rotational symmetry with two major peaks and two minor ones for BFO1.3, as shown in Figure 6d, and the peak positions have rotated away from the standard angles mentioned above. This indicates the change of polarization orientation and crystal structure. We consider a tetragonal structure in point group 4mm for the Bi-deficient BFO0.8 thin film, and the corresponding simulated curves are in good agreement with the experimental data as shown in Figure 6a,b. For the Bi-excess BFO1.3 sample, the SHG data can be fitted well using a monoclinic structure in point group m, as shown in Figure 6c,d. These results demonstrate that the Bi-deficient BFO0.8 thin film has a tetragonal structure and the BFO1.3 sample shows a monoclinic distortion, which is in agreement with the STEM observations. The observed structure distortion is accompanied by the ferroelectric polarization evolution with Bi nonstoichiometry, which suggests that the structure distortion may also be relevant to the as-grown polarization state.

Raman spectra have also been measured to reveal the structure information of BFO ultrathin films. Ultraviolet polarized Raman spectroscopy was performed because of its effectivity of detecting the weak signal of thin films on bulk substrates for its shorter penetration depth.[47] Even so, the obtained effective Raman signals for the BFO ultrathin films are very weak because of the ultrathin thickness. Figure 7 shows the Raman spectra of the BFO ultrathin films collected in $Z(XY)\bar{Z}$ scattering configurations. Only two peaks at 175 and 220 cm^{-1} are identifiable for the BFO thin films by comparing the spectra with that of the substrate. These two peaks are obvious for the Bi-excess BFO thin films, but they are very weak or almost vanished for the Bi-deficient BFO0.9 and BFO0.8 samples. The change of the Raman modes indicates the structural variation between the Bi-excess and Bi-deficient BFO thin films. The Raman selection rules for the rhombohedral, tetragonal, and monoclinic crystal structures of BFO are given in Table I in ref 48. According to the Raman selection rules, the Raman spectra collected in perpendicular $Z(XY)\bar{Z}$ scattering configurations will show E modes for the rhombohedral structure, A′ modes for the monoclinic structure, and no modes for the tetragonal structure. Therefore, in consideration of the TEM and SHG results, the Raman peaks observed in the Bi-excess BFO thin films can be ascribed to the monoclinic structure, which is consistent with the reported studies.[48−50] Weakening or absence of these peaks for Bi-deficient BFO thin films suggests a tetragonal structure for these films. Béa et al.[50] have reported a similar observation in BFO thin films with different thicknesses, and disappearance of the Raman peaks at thinner films has been attributed to the increased symmetry of the thin films because of the structure change from monoclinic to tetragonal. Thus, the structure evolution of BFO ultrathin films with Bi content is further confirmed by the Raman observation.

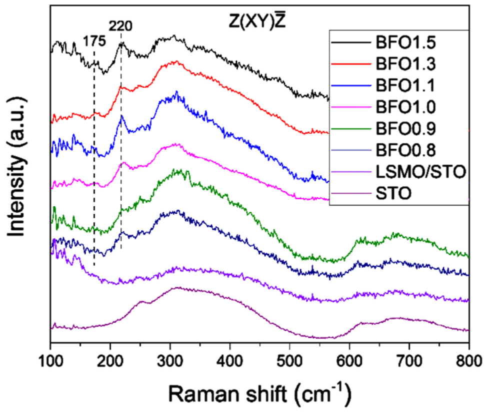

Figure 7. Ultraviolet Raman spectra of BFO ultrathin films collected in $Z(XY)\bar{Z}$ scattering configurations.

3.5. Modulation of the Band Gap of BFO Thin Films via Bi Nonstoichiometry. Spectroscopic ellipsometry has been employed to investigate the optical properties of BFO thin films. The real and imaginary dielectric constants or the optical parameters of refractive index n and extinction coefficient k versus photon energy can be extracted from the obtained ellipsometry parameters of Ψ and Δ. Figure 8 shows a

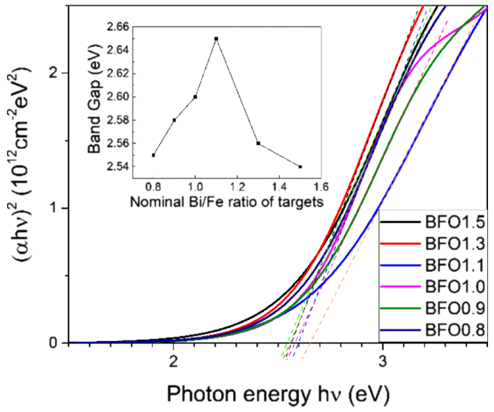

Figure 8. Plots of $(\alpha h\nu)^2$ vs photon energy of BFO ultrathin films. The inset shows the band gap variation of BFO ultrathin films with the nominal Bi/Fe ratio of BFO targets.

plot of $(\alpha h\nu)^2$ versus photon energy $h\nu$, where h is Plank's constant, ν is the frequency of illumination, and α is the absorption coefficient calculated by n and k. The band gap E_g can be obtained through the Tauc relation $(\alpha h\nu)^n = A(h\nu - E_g)$, where A is a constant and $n = 2$ for the direct band gap. The direct band gap values acquired by the linear extrapolation of $(\alpha h\nu)^2$ for BFO ultrathin films are shown in the inset of Figure 8. The BFO1.1 thin film that almost has an exact stoichiometric composition shows the largest band gap of 2.65 eV. Then, the band gap of thin films decreases with the increase of off-stoichiometry for both the Bi-excess and Bi-deficient films. In other words, the band gap of BFO thin films has been modulated to a narrow band gap by using either Bi-excess or Bi-deficient nonstoichiometry. The band gap of 2.65 eV is consistent with the reported values.[51,52] Ihlefeld et al.[51] have also observed a lower onset of optical absorption for the bismuth-deficient BFO film compared with the stoichiometric epitaxial film. For the existence of Bi nonstoichiometry, the BFO thin films would have various defects, such as Bi or Fe vacancies, oxygen vacancies, even some interstitial defects, and so forth. Those defects may give rise to p-type or n-type doping effects and various degrees of lattice distortion, all of which may contribute to the reduction of band gap.[53−57] Ferroelectric photovoltaic effects have attracted much attention for its unique light energy conversion based on polarization-driven carrier separation and above-band gap voltages.[56] However, ferroelectrics often have a wide band gap and then suffer from poor absorption of visible light. Therefore, the modulation of the band gap in BFO thin films via Bi nonstoichiometry will be valuable for the applications in photovoltaic and photocatalytic materials.

4. CONCLUSIONS

In summary, it has been observed that the ferroelectric polarization and crystal structure of BFO thin films can be manipulated artificially by controlling Bi nonstoichiometry. By decreasing the Bi/Fe ratio from excess Bi to deficient Bi, the as-grown polarization of BFO ultrathin films on LSMO-covered STO substrates can be changed completely from upward to downward orientation, and in the meantime, the surface morphology becomes better and eventually shows clear atomic steps and terraces in the Bi-deficient samples. High-resolution TEM, SHG measurements, and Raman spectra indicate that the upward polarization Bi-excess BFO thin film shows a monoclinic distortion with the $(MnO_2)^{0.7-}-(BiO)^{1+}$ interface atomic configuration, whereas the downward polarization Bi-deficient BFO thin film has a tetragonal structure with the $[(La_{0.7}Sr_{0.3})O]^{0.7+}-(FeO_2)^{1-}$ interface atomic configuration. The interface configuration, controlled by Bi concentration, should be mainly responsible for the as-grown polarization directions as well as the structural distortion. Moreover, it has been revealed that the band gap of BFO thin films can be modulated via Bi nonstoichiometry. Finally, we conclude that Bi nonstoichiometry plays a crucial role in structural distortion and ferroelectric domain state in the BFO thin films, and this study will be important for the design and fabrication of BFO-based thin-film devices.

■ ASSOCIATED CONTENT

Ⓢ Supporting Information

The Supporting Information is available free of charge on the ACS Publications website at DOI: 10.1021/acsami.8b15703.

Compositions of targets and films; X-ray absorption spectra; AFM images of STO substrate and LSMO/STO thin film; and low-magnification STEM images (PDF)

■ AUTHOR INFORMATION

Corresponding Authors

*E-mail: canwang@iphy.ac.cn (C.W.).
*E-mail: kjjin@iphy.ac.cn (K.J.).

ORCID

Can Wang: 0000-0002-4404-7957
Peng Gao: 0000-0003-0860-5525
Xuedong Bai: 0000-0002-1403-491X
Kuijuan Jin: 0000-0002-0047-4375

Notes

The authors declare no competing financial interest.

■ ACKNOWLEDGMENTS

This work was supported by the National Key R&D Program of China (no. 2017YFA0303604), the National Natural Science Foundation of China (nos. 11874412, 11674385, 11721404, and 11404380), and the Strategic Priority Research Program (B) of the Chinese Academy of Sciences (grant no. XDB07030200). The authors acknowledge the 4B9B beamline of Beijing Synchrotron Radiation Facility for technical support.

■ REFERENCES

(1) Scott, J. F. Applications of Modern Ferroelectrics. *Science* **2007**, *315*, 954−959.

(2) Cai, K.; Yang, M.; Ju, H.; Wang, S.; Ji, Y.; Li, B.; Edmonds, K. W.; Sheng, Y.; Zhang, B.; Zhang, N.; Liu, S.; Zheng, H.; Wang, K. Electric Field Control of Deterministic Current-Induced Magnetization Switching in a Hybrid Ferromagnetic/Ferroelectric Structure. *Nat. Mater.* **2017**, *16*, 712−716.

(3) McGilly, L. J.; Yudin, P.; Feigl, L.; Tagantsev, A. K.; Setter, N. Controlling Domain Wall Motion in Ferroelectric Thin Films. *Nat. Nanotechnol.* **2015**, *10*, 145−150.

(4) Jiang, J.; Bai, Z. L.; Chen, Z. H.; He, L.; Zhang, D. W.; Zhang, Q. H.; Shi, J. A.; Park, M. H.; Scott, J. F.; Hwang, C. S.; Jiang, A. Q. Temporary Formation of Highly Conducting Domain Walls for Non-Destructive Read-Out of Ferroelectric Domain-Wall Resistance Switching Memories. *Nat. Mater.* **2018**, *17*, 49−56.

(5) Seidel, J.; Martin, L. W.; He, Q.; Zhan, Q.; Chu, Y.-H.; Rother, A.; Hawkridge, M. E.; Maksymovych, P.; Yu, P.; Gajek, M.; Balke, N.; Kalinin, S. V.; Gemming, S.; Wang, F.; Catalan, G.; Scott, J. F.; Spaldin, N. A.; Orenstein, J.; Ramesh, R. Conduction at Domain Walls in Oxide Multiferroics. *Nat. Mater.* **2009**, *8*, 229−234.

(6) Ma, J.; Ma, J.; Zhang, Q.; Peng, R.; Wang, J.; Liu, C.; Wang, M.; Li, N.; Chen, M.; Cheng, X.; Gao, P.; Gu, L.; Chen, L.-Q.; Yu, P.; Zhang, J.; Nan, C.-W. Controllable Conductive Readout in Self-Assembled, Topologically Confined Ferroelectric Domain Walls. *Nat. Nanotechnol.* **2018**, *13*, 947−952.

(7) Cazorla, C.; Stengel, M. Electrostatic Engineering of Strained Ferroelectric Perovskites From First Principles. *Phys. Rev. B: Condens. Matter Mater. Phys.* **2015**, *92*, 214108.

(8) Schlom, D. G.; Chen, L.-Q.; Eom, C.-B.; Rabe, K. M.; Streiffer, S. K.; Triscone, J.-M. Strain Tuning of Ferroelectric Thin Films. *Annu. Rev. Mater. Res.* **2007**, *37*, 589−626.

(9) Yu, P.; Chu, Y.-H.; Ramesh, R. Oxide Interfaces: Pathways to Novel Phenomena. *Mater. Today* **2012**, *15*, 320−327.

(10) Yu, P.; Luo, W.; Yi, D.; Zhang, J. X.; Rossell, M. D.; Yang, C.-H.; You, L.; Singh-Bhalla, G.; Yang, S. Y.; He, Q.; Ramasse, Q. M.; Erni, R.; Martin, L. W.; Chu, Y. H.; Pantelides, S. T.; Pennycook, S. J.; Ramesh, R. Interface Control of Bulk Ferroelectric Polarization. *Proc. Natl. Acad. Sci. U.S.A.* **2012**, *109*, 9710−9715.

(11) Dutta, D. P.; Jayakumar, O. D.; Tyagi, A. K.; Girija, K. G.; Pillai, C. G. S.; Sharma, G. Effect of Doping on the Morphology and Multiferroic Properties of $BiFeO_3$ Nanorods. *Nanoscale* **2010**, *2*, 1149−1154.

(12) You, L.; Lu, C.; Yang, P.; Han, G.; Wu, T.; Luders, U.; Prellier, W.; Yao, K.; Chen, L.; Wang, J. Uniaxial Magnetic Anisotropy in $La_{0.7}Sr_{0.3}MnO_3$ Thin Films Induced by Multiferroic $BiFeO_3$ with Striped Ferroelectric Domains. *Adv. Mater.* **2010**, *22*, 4964−4968.

(13) Michel, C.; Moreau, J.-M.; Achenbach, G. D.; Gerson, R.; James, W. J. The Atomic Structure of $BiFeO_3$. *Solid State Commun.* **1969**, *7*, 701−704.

(14) Choi, T.; Lee, S.; Choi, Y. J.; Kiryukhin, V.; Cheong, S.-W. Switchable Ferroelectric Diode and Photovoltaic Effect in $BiFeO_3$. *Science* **2009**, *324*, 63−66.

(15) Kubel, F.; Schmid, H. Structure of a Ferroelectric and Ferroelastic Monodomain Crystal of the Perovskite $BiFeO_3$. *Acta Crystallogr., Sect. B: Struct. Sci.* **1990**, *46*, 698−702.

(16) Jang, H. W.; Baek, S. H.; Ortiz, D.; Folkman, C. M.; Das, R. R.; Chu, Y. H.; Shafer, P.; Zhang, J. X.; Choudhury, S.; Vaithyanathan, V.; Chen, Y. B.; Felker, D. A.; Biegalski, M. D.; Rzchowski, M. S.; Pan, X. Q.; Schlom, D. G.; Chen, L. Q.; Ramesh, R.; Eom, C. B. Strain-Induced Polarization Rotation in Epitaxial (001) $BiFeO_3$ Thin Films. *Phys. Rev. Lett.* **2008**, *101*, 107602.

(17) Christen, H. M.; Nam, J. H.; Kim, H. S.; Hatt, A. J.; Spaldin, N. A. Stress-Induced $R-M_A-M_C-T$ Symmetry Changes in $BiFeO_3$ Films. *Phys. Rev. B: Condens. Matter Mater. Phys.* **2011**, *83*, 144107.

(18) Jang, H. W.; Ortiz, D.; Baek, S.-H.; Folkman, C. M.; Das, R. R.; Shafer, P.; Chen, Y.; Nelson, C. T.; Pan, X.; Ramesh, R.; Eom, C.-B. Domain Engineering for Enhanced Ferroelectric Properties of Epitaxial (001) $BiFeO_3$ Thin Films. *Adv. Mater.* **2009**, *21*, 817−823.

(19) Chen, Z.; Luo, Z.; Huang, C.; Qi, Y.; Yang, P.; You, L.; Hu, C.; Wu, T.; Wang, J.; Gao, C.; Sritharan, T.; Chen, L. Low-Symmetry Monoclinic Phases and Polarization Rotation Path Mediated by Epitaxial Strain in Multiferroic $BiFeO_3$ Thin Films. *Adv. Funct. Mater.* **2011**, *21*, 133−138.

(20) Zeches, R. J.; Rossell, M. D.; Zhang, J. X.; Hatt, A. J.; He, Q.; Yang, C.-H.; Kumar, A.; Wang, C. H.; Melville, A.; Adamo, C.; Sheng, G.; Chu, Y.-H.; Ihlefeld, J. F.; Erni, R.; Ederer, C.; Gopalan, V.; Chen, L. Q.; Schlom, D. G.; Spaldin, N. A.; Martin, L. W.; Ramesh, R. A Strain-Driven Morphotropic Phase Boundary in $BiFeO_3$. *Science* **2009**, *326*, 977−980.

(21) Jeon, B. C.; Lee, D.; Lee, M. H.; Yang, S. M.; Chae, S. C.; Song, T. K.; Bu, S. D.; Chung, J.-S.; Yoon, J.-G.; Noh, T. W. Flexoelectric Effect in the Reversal of Self-Polarization and Associated Changes in the Electronic Functional Properties of $BiFeO_3$ Thin Films. *Adv. Mater.* **2013**, *25*, 5643−5649.

(22) Catalan, G.; Lubk, A.; Vlooswijk, A. H. G.; Snoeck, E.; Magen, C.; Janssens, A.; Rispens, G.; Rijnders, G.; Blank, D. H. A.; Noheda, B. Flexoelectric Rotation of Polarization in Ferroelectric Thin Films. *Nat. Mater.* **2011**, *10*, 963−967.

(23) Lee, D.; Yoon, A.; Jang, S. Y.; Yoon, J.-G.; Chung, J.-S.; Kim, M.; Scott, J. F.; Noh, T. W. Giant Flexoelectric Effect in Ferroelectric Epitaxial Thin Films. *Phys. Rev. Lett.* **2011**, *107*, 057602.

(24) Paudel, T. R.; Jaswal, S. S.; Tsymbal, E. Y. Intrinsic Defects in Multiferroic $BiFeO_3$ and Their Effect on Magnetism. *Phys. Rev. B: Condens. Matter Mater. Phys.* **2012**, *85*, 104409.

(25) Lee, J. H.; Jeon, J. H.; Yoon, C.; Lee, S.; Kim, Y. S.; Oh, T. J.; Kim, Y. H.; Park, J.; Song, T. K.; Park, B. H. Intrinsic Defect-Mediated Conduction and Resistive Switching in Multiferroic $BiFeO_3$ Thin Films Epitaxially Grown on $SrRuO_3$ Bottom Electrodes. *Appl. Phys. Lett.* **2016**, *108*, 112902.

(26) Wu, J.; Wang, J.; Xiao, D.; Zhu, J. A Method to Improve Electrical Properties of BiFeO3 Thin Films. *ACS Appl. Mater. Interfaces* **2012**, *4*, 1182−1185.

(27) Dedon, L. R.; Saremi, S.; Chen, Z.; Damodaran, A. R.; Apgar, B. A.; Gao, R.; Martin, L. W. Nonstoichiometry, Structure, and Properties of BiFeO3 Films. *Chem. Mater.* **2016**, *28*, 5952−5961.

(28) Hu, W. J.; Wang, Z.; Yu, W.; Wu, T. Optically Controlled Electroresistance And Electrically Controlled Photovoltage in Ferroelectric Tunnel Junctions. *Nat. Commun.* **2016**, *7*, 10808.

(29) Yamada, H.; Garcia, V.; Fusil, S.; Boyn, S.; Marinova, M.; Gloter, A.; Xavier, S.; Grollier, J.; Jacquet, E.; Carrétéro, C.; Deranlot, C.; Bibes, M.; Barthélémy, A. Giant Electroresistance of Super-tetragonal $BiFeO_3$-Based Ferroelectric Tunnel Junctions. *ACS Nano* **2013**, *7*, 5385−5390.

(30) Liu, Y. K.; Yin, Y. W.; Dong, S. N.; Yang, S. W.; Jiang, T.; Li, X. G. Coexistence of Four Resistance States and Exchange Bias in $La_{0.6}Sr_{0.4}MnO_3/BiFeO_3/La_{0.6}Sr_{0.4}MnO_3$ Multiferroic Tunnel Junction. *Appl. Phys. Lett.* **2014**, *104*, 043507.

(31) Feng, Y.; Wang, C.; Tian, S.; Zhou, Y.; Ge, C.; Guo, H.; He, M.; Jin, K.; Yang, G. Controllable Growth of Ultrathin $BiFeO_3$ From Finger-Like Nanostripes to Atomically Flat Films. *Nanotechnology* **2016**, *27*, 355604.

(32) Guo, H.; Zhao, R.; Jin, K.-j.; Gu, L.; Xiao, D.; Yang, Z.; Li, X.; Wang, L.; He, X.; Gu, J.; Wan, Q.; Wang, C.; Lu, H.; Ge, C.; He, M.; Yang, G. Interfacial-Strain-Induced Structural and Polarization Evolutions in Epitaxial Multiferroic $BiFeO_3$ (001) Thin Films. *ACS Appl. Mater. Interfaces* **2015**, *7*, 2944−2951.

(33) Kim, D. H.; Lee, H. N.; Biegalski, M. D.; Christen, H. M. Effect of Epitaxial Strain on Ferroelectric Polarization in Multiferroic $BiFeO_3$ Films. *Appl. Phys. Lett.* **2008**, *92*, 012911.

(34) Chu, Y. H.; Zhao, T.; Cruz, M. P.; Zhan, Q.; Yang, P. L.; Martin, L. W.; Huijben, M.; Yang, C. H.; Zavaliche, F.; Zheng, H.; Ramesh, R. Ferroelectric Size Effects in Multiferroic $BiFeO_3$ Thin Films. *Appl. Phys. Lett.* **2007**, *90*, 252906.

(35) Deepak, N.; Carolan, P.; Keeney, L.; Zhang, P. F.; Pemble, M. E.; Whatmore, R. W. Bismuth Self-Limiting Growth of Ultrathin $BiFeO_3$ Films. *Chem. Mater.* **2015**, *27*, 6508−6515.

(36) Fujisawa, H.; Yoshimura, N.; Nakashima, S.; Shimizu, M. Self-regulation of Bi/(Bi+Fe) Ratio in Metal organic Chemical Vapor Deposition of $BiFeO_3$ Thin Films. *Jpn. J. Appl. Phys.* **2017**, *56*, 10PF05.

(37) Vanka, S. P.; Luo, G.; Glumac, N. G. Parametric Effects on Thin Film Growth and Uniformity in an Atmospheric Pressure Impinging Jet CVD Reactor. *J. Cryst. Growth* **2004**, *267*, 22−34.

(38) Chen, Z.; Luo, Z.; Qi, Y.; Yang, P.; Wu, S.; Huang, C.; Wu, T.; Wang, J.; Gao, C.; Sritharan, T.; Chen, L. Low Symmetry Monoclinic MC Phase in Epitaxial $BiFeO_3$ Thin Films on $LaSrAlO_4$ Substrates. *Appl. Phys. Lett.* **2010**, *97*, 242903.

(39) Béa, H.; Bibes, M.; Barthélémy, A.; Bouzehouane, K.; Jacquet, E.; Khodan, A.; Contour, J.-P.; Fusil, S.; Wyczisk, F.; Forget, A.; Lebeugle, D.; Colson, D.; Viret, M. Influence of Parasitic Phases on the Properties of $BiFeO_3$ Epitaxial Thin Films. *Appl. Phys. Lett.* **2005**, *87*, 072508.

(40) You, L.; Chua, N. T.; Yao, K.; Chen, L.; Wang, J. Influence of Oxygen Pressure on the Ferroelectric Properties of Epitaxial $BiFeO_3$ Thin Films by Pulsed Laser Deposition. *Phys. Rev. B: Condens. Matter Mater. Phys.* **2009**, *80*, 024105.

(41) Ohtomo, A.; Hwang, H. Y. A High-Mobility Electron Gas at the $LaAlO_3/SrTiO_3$ Heterointerface. *Nature* **2004**, *427*, 423−426.

(42) Yu, P.; Lee, J.-S.; Okamoto, S.; Rossell, M. D.; Huijben, M.; Yang, C.-H.; He, Q.; Zhang, J. X.; Yang, S. Y.; Lee, M. J.; Ramasse, Q. M.; Erni, R.; Chu, Y.-H.; Arena, D. A.; Kao, C.-C.; Martin, L. W.; Ramesh, R. Interface Ferromagnetism and Orbital Reconstruction in $BiFeO_3$-$La_{0.7}Sr_{0.3}MnO_3$ Heterostructures. *Phys. Rev. Lett.* **2010**, *105*, 027201.

(43) Trassin, M.; Luca, G. D.; Manz, S.; Fiebig, M. Probing Ferroelectric Domain Engineering in $BiFeO_3$ Thin Films by Second Harmonic Generation. *Adv. Mater.* **2015**, *27*, 4871−4876.

(44) Kumar, A.; Denev, S.; Zeches, R. J.; Vlahos, E.; Podraza, N. J.; Melville, A.; Schlom, D. G.; Ramesh, R.; Gopalan, V. Probing Mixed Tetragonal/Rhombohedral-Like Monoclinic Phases in Strained Bismuth Ferrite Films by Optical Second Harmonic Generation. *Appl. Phys. Lett.* **2010**, *97*, 112903.

DOI: 10.1021/acsami.8b15703
ACS Appl. Mater. Interfaces 2018, 10, 43792−43801

(45) Denev, S. A.; Lummen, T. T. A.; Barnes, E.; Kumar, A.; Gopalan, V. Probing Ferroelectrics Using Optical Second Harmonic Generation. *J. Am. Ceram. Soc.* **2011**, *94*, 2699−2727.

(46) Wang, J.-S.; Jin, K.-J.; Guo, H.-Z.; Gu, J.-X.; Wan, Q.; He, X.; Li, X.-L.; Xu, X.-L.; Yang, G.-Z. Evolution of Structural Distortion in BiFeO3 Thin Films Probed by Second-Harmonic Generation. *Sci. Rep.* **2016**, *6*, 38268.

(47) Tenne, D. A.; Bruchhausen, A.; Lanzillotti-Kimura, N. D.; Fainstein, A.; Katiyar, R. S.; Cantarero, A.; Soukiassian, A.; Vaithyanathan, V.; Haeni, J. H.; Tian, W.; Schlom, D. G.; Choi, K. J.; Kim, D. M.; Eom, C. B.; Sun, H. P.; Pan, X. Q.; Li, Y. L.; Chen, L. Q.; Jia, Q. X.; Nakhmanson, S. M.; Rabe, K. M.; Xi, X. X. Probing Nanoscale Ferroelectricity by Ultraviolet Raman Spectroscopy. *Science* **2006**, *313*, 1614−1616.

(48) Palai, R.; Katiyar, R. S.; Schmid, H.; Tissot, P.; Clark, S. J.; Robertson, J.; Redfern, S. A. T.; Catalan, G.; Scott, J. F. β Phase and γ-β Metal-Insulator Transition in Multiferroic $BiFeO_3$. *Phys. Rev. B: Condens. Matter Mater. Phys.* **2008**, *77*, 014110.

(49) Palai, R.; Schmid, H.; Scott, J. F.; Katiyar, R. S. Raman Spectroscopy of Single-Domain Multiferroic $BiFeO_3$. *Phys. Rev. B: Condens. Matter Mater. Phys.* **2010**, *81*, 064110.

(50) Béa, H.; Bibes, M.; Petit, S.; Kreisel, J.; Barthélémy, A. Structural Distortion and Magnetism of $BiFeO_3$ Epitaxial Thin Films: A Raman Spectroscopy and Neutron Diffraction Study. *Philos. Mag. Lett.* **2007**, *87*, 165−174.

(51) Ihlefeld, J. F.; Podraza, N. J.; Liu, Z. K.; Rai, R. C.; Xu, X.; Heeg, T.; Chen, Y. B.; Li, J.; Collins, R. W.; Musfeldt, J. L.; Pan, X. Q.; Schubert, J.; Ramesh, R.; Schlom, D. G. Optical Band Gap of $BiFeO_3$ Grown by Molecular-Beam Epitaxy. *Appl. Phys. Lett.* **2008**, *92*, 142908.

(52) Ji, W.; Yao, K.; Liang, Y. C. Bulk Photovoltaic Effect at Visible Wavelength in Epitaxial Ferroelectric $BiFeO_3$ Thin Films. *Adv. Mater.* **2010**, *22*, 1763−1766.

(53) Mocherla, P. S. V.; Karthik, C.; Ubic, R.; Rao, M. S. R.; Sudakar, C. Tunable Bandgap in $BiFeO_3$ Nanoparticles: The Role of Microstrain and Oxygen Defects. *Appl. Phys. Lett.* **2013**, *103*, 022910.

(54) Gómez-Salces, S.; Aguado, F.; Rodríguez, F.; Valiente, R.; González, J.; Haumont, R.; Kreisel, J. Effect of Pressure on the Band Gap and the Local FeO_6 Environment in $BiFeO_3$. *Phys. Rev. B: Condens. Matter Mater. Phys.* **2012**, *85*, 144109.

(55) Zhang, H.; Liu, W.; Wu, P.; Hai, X.; Guo, M.; Xi, X.; Gao, J.; Wang, X.; Guo, F.; Xu, X.; Wang, C.; Liu, G.; Chu, W.; Wang, S. Novel Behaviors of Multiferroic Properties in Na-Doped $BiFeO_3$ Nanoparticles. *Nanoscale* **2014**, *6*, 10831−10838.

(56) Yang, S. Y.; Seidel, J.; Byrnes, S. J.; Shafer, P.; Yang, C.-H.; Rossell, M. D.; Yu, P.; Chu, Y.-H.; Scott, J. F.; Ager, J. W., 3rd; Martin, L. W.; Ramesh, R. Above-Bandgap Voltages from Ferroelectric Photovoltaic Devices. *Nat. Nanotechnol.* **2010**, *5*, 143−147.

(57) Nechache, R.; Harnagea, C.; Li, S.; Cardenas, L.; Huang, W.; Chakrabartty, J.; Rosei, F. Bandgap Tuning of Multiferroic Oxide Solar Cells. *Nat. Photonics* **2014**, *9*, 61−67.